CHEMISTRY OF MATERIALS

pubs.acs.org/cm

Article

Influence of Metastable Disorder in Titanium Oxyhydroxides on High-Rate Sodium Ion Storage

Dnyanesh Vernekar,[⊥] Soumyajit Gupta,[⊥] Gi-Hyeok Lee, Reshma Devi, Mohamed Ruwaid Rafiuddin, Gopalakrishnan Sai Gautam, Wanli Yang, and Srinivasan Ramakrishnan*

Cite This: https://doi.org/10.1021/acs.chemmater.6c00507

Read Online

ACCESS | Metrics & More | Article Recommendations | Supporting Information

ABSTRACT: The inability of graphite to store Na^+ ions at low potentials necessitates the use of disordered materials as anodes in Na-ion batteries, wherein complex degradative pathways limit cycle life. This study delineates the influence of synthetically induced material disorder in facilitating stable, high-rate sodium ion storage in a series of anatase titania analogs. The degree of disorder in the titanium oxyhydroxide ($TiO_x(OH)_y$-T_{anneal}) materials, synthesized via a simple, solution-phase sol−gel protocol employing a Ti(III) precursor, is systematically varied by tuning the postsynthesis annealing temperature (T_{anneal}). The variable disorder in $TiO_x(OH)_y$-T_{anneal} stems from the distribution of residual Ti(III), N-dopants, and O-vacancies in these materials as a function of T_{anneal}, as mapped by XPS, bulk-sensitive resonance inelastic X-ray scattering (RIXS), and EPR spectroscopy. In terms of electrochemical performance, we observe a unique, nonmonotonic dependence of Na^+ storage capacity on the synthetically induced degree of disorder in $TiO_x(OH)_y$-T_{anneal}, instead of a simple inverse size dependence, as normally seen in the case of fully crystalline anatase materials. Further in contrast to crystalline anatase, the disorder in $TiO_x(OH)_y$-T_{anneal} opens up a bulk mode of Na^+ storage instead of a purely surface confined or capacitive mode, as determined by scan rate-dependent cyclic voltammetry. $TiO_x(OH)_y$-400, with an intermediary amount of disorder in the prepared series of materials, shows the highest specific capacity (~188 mAh/g) and cycling stability for Na^+ storage at elevated rates. These results are in agreement with our first-principles simulated data exhibiting a higher number of possible sites that Na^+ can occupy at an intermediate degree of disorder in a $TiO_x(OH)_y$ structure.

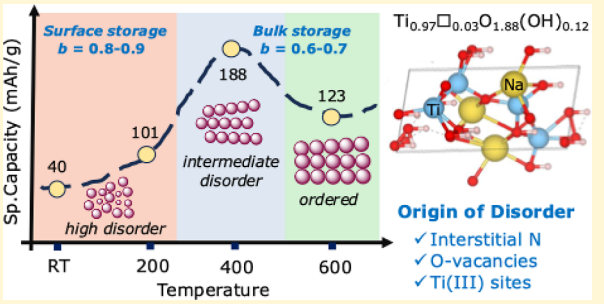

1. INTRODUCTION

The intermittency of renewable energy sources such as solar and wind necessitates the adoption of inexpensive storage solutions at the GW scale.[1] Rechargeable sodium-ion batteries (SIBs) are promising candidates for such applications due to their similarity in manufacturing to Li-ion batteries, lower reliance on critical minerals, and nominal energy density.[2,3] Despite their similarity to Li-ion, several challenges centered around cathodic, anodic, as well as interfacial instabilities remain, which limits their long-term cyclability.[4,5] As graphite cannot be used to store Na^+ ions at low potentials,[6,7] disordered materials such as hard carbon are often employed as anodes in SIBs.[8] Despite possessing a high specific capacity for sodium storage (250−300 mAh/g), long-term cyclability has been a challenge in hard carbons due to significant microstructural variabilities arising from differences in their biomass precursors and/or synthesis conditions.[9,10] Furthermore, since a significant fraction of the capacity in hard carbon originates below 0.1 V vs $Na^{+/0}$,[11] operating at high charging currents can induce Na plating, thus, raising safety concerns.

Titania (TiO_2)-based materials have attracted interest as anodes due to their abundance, ease of synthesis, and the corresponding ability to modulate electronic structure, as well as nominal storage capacity for alkali metal ions such as Li^+ and Na^+.[12−14] While their specific capacity can be a function of several factors including particle size and exposed crystallographic facets, they display a sloping voltage profile during Na^+ insertion throughout the voltage window, unlike the high-voltage plateau observed during Li insertion (~1.75 V vs $Li^{+/0}$).[15−17] To improve the specific capacity of crystalline TiO_2 particles, nanosizing has been demonstrated to be an effective strategy, with gravimetric capacities approaching 200 mAh/g with sub-10 nm sized TiO_2.[18] The smaller size can improve Na^+ diffusivities and buffer mechanical stresses during repeated cycling.[19−21] Additional modifications such as doping, defect engineering, and external carbon coatings can improve

Received: February 17, 2026
Revised: March 18, 2026
Accepted: March 23, 2026

Scheme 1. Aqueous Solution-Phase Synthesis Route for $TiO_x(OH)_y$-T_{anneal}

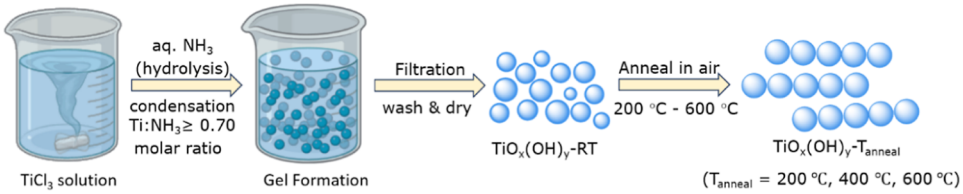

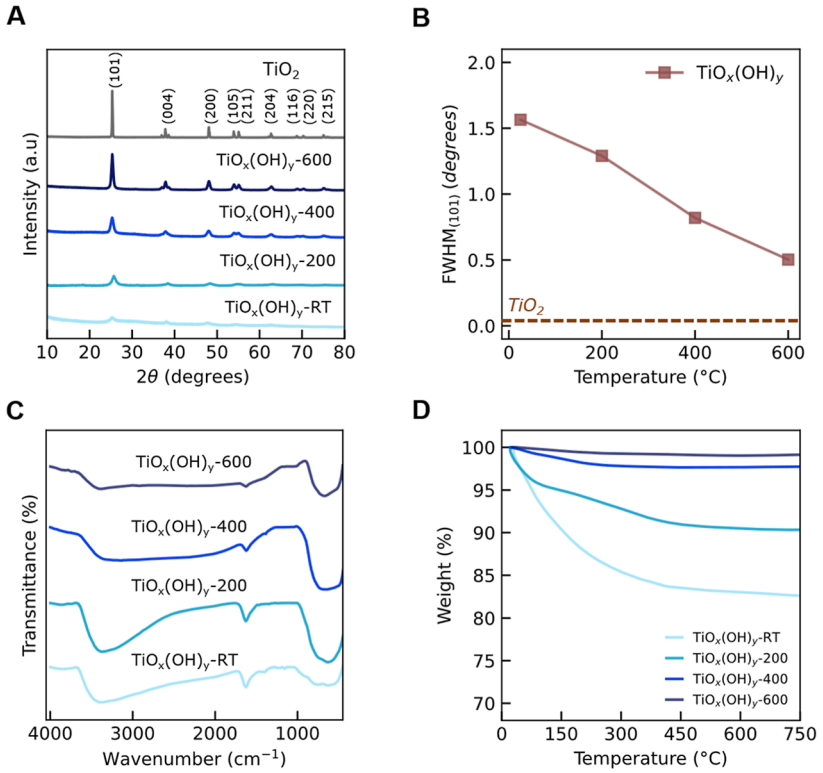

Figure 1. (A) pXRD spectra; (B) variation of the fwhm of the (101) peak; (C) Fourier transform infrared (FTIR) spectra, and (D) TGA data for the various $TiO_x(OH)_y$-T_{anneal} samples.

their electrical conductivity and overall electrochemical performance.[22]

The sodium storage mechanism in anatase TiO_2 consists of a combination of insertion, conversion, and pseudocapacitive pathways[23] with concomitant $Ti^{4+/3+}$ redox, and an expansion of the interslab spacing.[18,24] In the fully sodiated state, below 0.3 V vs $Na^{+/0}$, there is a notable loss of crystallinity of the parent anatase structure, with some partial recovery upon desodiation.[25,26] As a result, the sodium insertion/deinsertion in the subsequent cycles takes place in the disordered amorphous Na_xTiO_2 domains resulting from cation mixing between Ti and Na upon sodiation.[27] Upon desodiation, the structure transforms into a highly distorted 3D network, while maintaining local anatase structure.[27] Subsequent reversible sodiation/desodiation occurs between these two phases with a sloping voltage profile characteristic of a solid solution type of mechanism.[28]

Recently, it has been reported that the extent of amorphization in crystalline anatase is closely related to particle size,[16] with initial sodiation generating a thin (3−5 nm thick) amorphous layer. Such partial amorphization resulting in a core−shell structure can be disadvantageous in terms of the specific capacity for larger particles. Furthermore, kinetic studies in anatase nanocrystals through scan-rate-dependent cyclic voltammetry (CV) suggest that sodium storage is predominantly surface-confined irrespective of particle size, unlike the faradaic mode of charge storage typically observed in case of lithium insertion.[16] The unique mechanism of Na^+ storage in anatase and the purported effect of material disorder, therefore, highlight the need to systematically control the extent of disorder for achieving high-rate cyclability.

Disorder in TiO_2 can stem from the presence of dopants, cationic or anionic vacancies, and, which can influence Na^+ mobility and transport kinetics, potentially facilitating high-rate performance.[13,29,30] However, excessive structural disorder can impede long distance ion or electron transfer pathways, thereby, decreasing their high-rate electrochemical performance.[31] Hence, ensuring an optimal amount of disorder in the material could be beneficial for achieving ideal electronic and ionic conductivity.

Herein, we report a series of titanium oxyhydroxide materials ($TiO_x(OH)_y$-T_{anneal}) with synthetically tunable extents of disorder screened for their high-rate Na-ion storage capability. The specific capacity as a function of particle size in $TiO_x(OH)_y$-T_{anneal} materials with inherent porosity and disorder deviated from the inverse size dependence observed in case of fully crystalline anatase TiO_2. The high specific capacity (~188 mAh/g) at elevated rates is posited to derive

https://doi.org/10.1021/acs.chemmater.6c00507
Chem. Mater. XXXX, XXX, XXX−XXX

Table 1. Rietveld Refinement Results for the Different $TiO_x(OH)_y$ Materials[a]

S. No.	sample	a(Å)	c(Å)	titanium site occupancy	cation vacancy, p	composition
1	$TiO_x(OH)_y$-RT	3.812 (1)	9.490 (3)	0.7690	0.23 (0.03)	$Ti_{0.77}\square_{0.23}O_{1.08}(OH)_{0.92}$
2	$TiO_x(OH)_y$-200	3.796 (1)	9.476 (3)	0.9068	0.09 (0.02)	$Ti_{0.91}\square_{0.09}O_{1.64}(OH)_{0.36}$
3	$TiO_x(OH)_y$-400	3.788 (1)	9.497 (4)	0.9737	0.03 (0.02)	$Ti_{0.97}\square_{0.03}O_{1.88}(OH)_{0.12}$
4	$TiO_x(OH)_y$-600	3.786 (7)	9.505 (2)	1.0000	0	TiO_2

[a]The numbers in parentheses indicate the error bars.

from a bulk-mode Na^+ storage that is operative in $TiO_x(OH)_y$-400, which possesses an intermediary amount of disorder in the series of materials studied. Detailed electrochemical, spectroscopic, and computational studies delineate the origin and role of disorder and the associated electrochemical behavior.

2. RESULTS AND DISCUSSION

2.1. Synthesis and Physiochemical Properties of Titanium Oxyhydroxides

The titanium oxyhydroxides ($TiO_x(OH)_y$) were synthesized via a sol−gel protocol involving the controlled hydrolysis of an aqueous, acidic solution of $TiCl_3$ (pH = 0.2) using aq. NH_3 under ambient conditions (Scheme 1, see Experimental Section Details). The solution initially turned deep blue upon NH_3 addition, presumably due to the formation of a $Ti(NH_3)_xCl_y$ complex, subsequently leading to a white precipitate, viz. the titanium oxyhydroxide precursor "$TiO_x(OH)_y$-RT" upon further hydrolysis. The Ti^{3+}/NH_3 molar ratio during the synthesis of $TiO_x(OH)_y$ was maintained above 0.7, below which the formation of a fully amorphous material was observed. The $TiO_x(OH)_y$ precipitate was sequentially washed with deionized water, isopropanol, and acetone, respectively, and dried at 80 °C. The $TiO_x(OH)_y$-RT was then divided into batches and annealed to different temperatures ("T_{anneal}") ranging from 200 to 600 °C for 4 h in air yielding the corresponding variants, viz. $TiO_x(OH)_y$-200, $TiO_x(OH)_y$-400, and $TiO_x(OH)_y$-600, respectively.

The powder X-ray diffraction (pXRD) data for the nonannealed material, $TiO_x(OH)_y$-RT, showed broad peaks corresponding to the anatase phase of TiO_2, pointing to a partially amorphous/semicrystalline nature (Figure 1A). These peaks grew sharper with a concomitant decrease in the fwhm (Figure 1B) upon annealing, eventually converging to a nominally crystalline anatase TiO_2 phase[32] in $TiO_x(OH)_y$-600. The larger fwhm in the $TiO_x(OH)_y$-T_{anneal} samples compared to commercial anatase TiO_2 indicated a progressively greater degree of disorder inversely correlated with T_{anneal} (Figure 1B). Even for $TiO_x(OH)_y$-600, the fwhm of the most intense (101) peak was found to be higher than that of the commercial anatase sample, indicating the presence of some residual disorder, albeit to a lesser degree compared to the lower temperature congeners. Notably these trends were found to be reproducible across different batch sizes (Figure S1).

The pXRD data of the $TiO_x(OH)_y$-T_{anneal} samples (RT, 200 °C, 400 °C, and 600 °C) were refined using a structural model of anatase TiO_2 in order to obtain the lattice parameters and the site occupancy factors of Ti. Rietveld analysis confirmed that the synthesized materials adopt the anatase structure, and the refinement results are shown in Table 1 and Figure S2. The refinement results indicated the presence of significant cationic vacancies for $TiO_x(OH)_y$-RT that decrease with T_{anneal} (Table 1), likely to compensate for the negative charge deficiency caused by the substitution of O^{2-} by OH^-.[33] Taking the cationic vacancies into account, a general chemical formula of $Ti_{1-x}\square_xO_{2-4x}OH_{4x}$ can be proposed.[33] Rietveld analysis indicated the presence of 23%, 9%, and 3% cationic vacancies for the $TiO_x(OH)_y$-RT, $TiO_x(OH)_y$-200, and $TiO_x(OH)_y$-400 samples, respectively. It must be noted here that with the given resolution of the pXRD data, the Rietveld analysis could not ascribe cationic vacancies to $TiO_x(OH)_y$-600, which indicates near complete removal of the OH^- moieties. Hence, the chemical composition of the nonannealed sample was found to be $Ti_{0.77}\square_{0.23}O_{1.08}(OH)_{0.92}$ while the samples annealed to 200 °C, 400 °C, and 600 °C have chemical compositions $Ti_{0.91}\square_{0.09}O_{1.64}(OH)_{0.36}$, $Ti_{0.97}\square_{0.03}O_{1.88}(OH)_{0.12}$, and TiO_2, respectively (Table 1). With increasing T_{anneal}, an anisotropic change in the unit cell parameters was observed, i.e., the "a" parameter decreases while the "c" parameter increases with increasing T_{anneal} (Figure S3), akin to previous reports which ascribe such shifts to Ti vacancies.[34,35]

The coordination environment around Ti was analyzed using FTIR spectroscopy (Figure 1C). A broad absorption band centered around 3400 cm^{-1} was observed in all the $TiO_x(OH)_y$-T_{anneal} samples, which was assigned to the stretching vibration of surface hydroxyl groups (−OH) and adsorbed water molecules.[36,37] Further, the broad envelope of this feature is posited to contain peaks originating from Ti−OH stretching vibrations that are typically observed around 2920 cm^{-1} and 2840 cm^{-1}.[38] The sharp feature around 1626 cm^{-1}, usually assigned to hydrogen-bonded water molecules physiosorbed onto TiOH or $Ti(OH)_2$ groups, was observed in all our $TiO_x(OH)_y$-T_{anneal} samples.[39] The intensity of all these features monotonically decreased with T_{anneal}, indicating a loss of such moieties at elevated temperatures.[40] The loss of such moieties with increasing T_{anneal} is posited to decrease the structural disorder in the material, driving its transformation to crystalline anatase, as evidenced by the pXRD data. Further, Ti−O−Ti vibrational modes were also observed in the FTIR between 1000 and 400 cm^{-1}, which are characteristic features of titania-based materials, and were found to be largely invariant with T_{anneal}.[41] Consistent with the FTIR data, the total mass loss observed by TGA in the $TiO_x(OH)_y$-T_{anneal} materials between 25 and 750 °C (Figure 1D) scaled inversely with T_{anneal} (Table 2). The pXRD, FTIR, and TGA results, therefore, point to a progressive decrease in disorder with T_{anneal} in the $TiO_x(OH)_y$-T_{anneal} materials.

The $TiO_x(OH)_y$ materials were further characterized with high-resolution transmission electron microscopy (Figure 2). The particle size of $TiO_x(OH)_y$-RT was less than 5 nm, with no noticeable agglomeration, confirming the effectiveness of the synthesis protocol in achieving a uniform distribution of nanoparticles without the use of any structure-directing agents. Upon annealing, an increase in the particle size was observed, presumably via Ostwald ripening, which was proportional to the T_{anneal} (Table 2). The mean particle size of $TiO_x(OH)_y$-

https://doi.org/10.1021/acs.chemmater.6c00507
Chem. Mater. XXXX, XXX, XXX−XXX

Table 2. Thermogravimetry, Size, and Surface Area Measurements of $TiO_x(OH)_y$-T_{anneal} Samples

S. No.	sample	mass loss (%)	average size (nm)	S_{BET} (m^2/g)	pore volume (cc/g)
1	$TiO_x(OH)_y$-RT	17.3	<5	370.1	0.404
2	$TiO_x(OH)_y$-200	9.6	6	244.3	0.316
3	$TiO_x(OH)_y$-400	2.3	11	120.6	0.373
4	$TiO_x(OH)_y$-600	0.9	32	78.0	0.273

600 was around 32 nm, which was similar to the corresponding value for the commercial anatase TiO_2 powder, viz. ∼31 nm. Increasing the annealing time beyond 4 h had no appreciable effect on the particle sizes or their uniformity. In the selected area electron diffraction (SAED) data, the diffuse rings observed for $TiO_x(OH)_y$-RT and $TiO_x(OH)_y$-200 (Figure 2A,B inset) clearly pointed to the higher degree of disorder as compared to the more crystalline $TiO_x(OH)_y$-400 and $TiO_x(OH)_y$-600 samples, in whose case sharper concentric rings were observed (Figure 2C,D insets). The interplanar distances determined from the SAED patterns were found to be 0.352 and 0.238 nm for $TiO_x(OH)_y$-600, corresponding to the (101) and (004) reflection planes, respectively. In contrast, $TiO_x(OH)_y$-400 exhibited marginally smaller *d*-spacing values of 0.342 and 0.230 nm, corresponding to the same planes. The surface area of these materials as determined from Brunauer–Emmett–Teller (BET) N_2 adsorption studies[42] also scaled inversely with annealing temperature (Figure S4A). While the nonannealed $TiO_x(OH)_y$-RT had a surface area of ∼370.1 m^2/g, the respective surface area for the material annealed to 600 °C was ∼78.0 m^2/g (Table 2). The pore volume estimated using the Barrett–Joyner–Halenda (BJH) method[43] also showed a decrease upon annealing (Table 2, Figure S4B) pointing to a decrease in material porosity accompanied by a gradual loss of structural disorder (vide supra). The slight increase in the pore volume from $TiO_x(OH)_y$-200 to $TiO_x(OH)_y$-400 could be attributed to structural reorganization from the evolution of mixed valent Ti-sites during annealing that levels off at higher temperatures (vide infra).

Further insights into the material composition and disorder in $TiO_x(OH)_y$-T_{anneal} were derived from spectroscopic analyses. A peak centered at a binding energy (BE) of 401 eV was observed in the N 1s XPS spectra of the nonannealed $TiO_x(OH)_y$-RT sample (Figure 3A). This peak was assigned to interstitial nitrogen species doped into the $TiO_x(OH)_y$ matrix,[44] likely originating from NH_3 employed in the synthesis protocol. The N 1s peak reduced in intensity as a function of T_{anneal} suggesting a progressive loss of nitrogen species from the $TiO_x(OH)_y$ matrix. The N content was found to be ∼1.51, ∼0.51, and ∼0.35% by weight in $TiO_x(OH)_y$-RT, $TiO_x(OH)_y$-200, and $TiO_x(OH)_y$-400, respectively, by CHNS analysis (Figure 3B), with no detectable N-containing species in $TiO_x(OH)_y$-600. The significant loss of N upon annealing suggested the presence of weakly held interstitial N within the Ti–O–Ti matrix. The presence of this interstitial N is expected to lead to local disorder affecting the regular atomic arrangement owing to its strong interaction with nearby

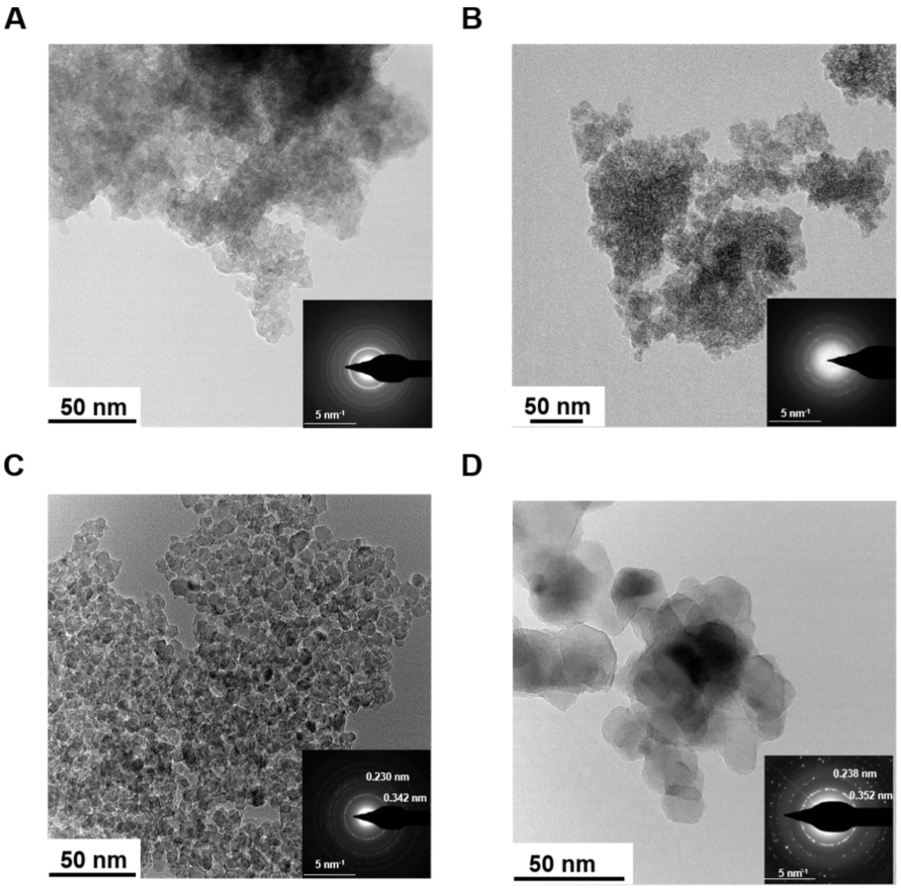

Figure 2. HRTEM images and SAED patterns (insets) for (A) $TiO_x(OH)_y$-RT, (B) $TiO_x(OH)_y$-200, (C) $TiO_x(OH)_y$-400, and (D) $TiO_x(OH)_y$-600.

https://doi.org/10.1021/acs.chemmater.6c00507
Chem. Mater. XXXX, XXX, XXX−XXX

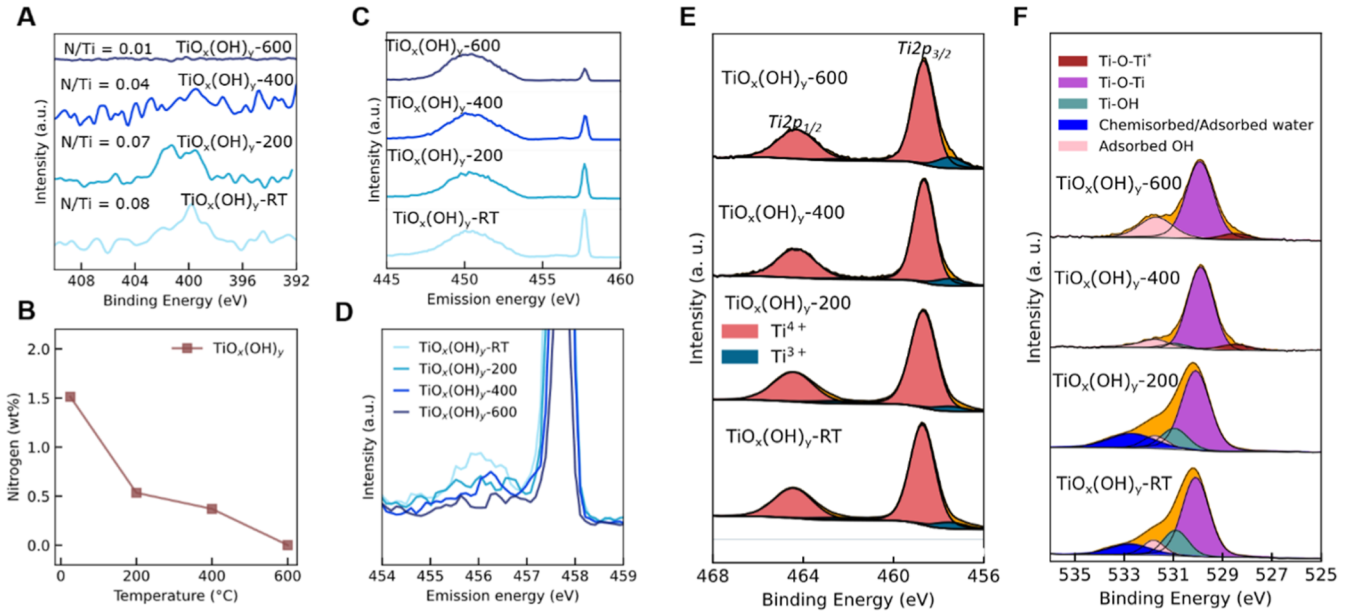

Figure 3. (A) N 1s XPS spectra ; (B) weight % of nitrogen from CHNS; (C) Ti-L_3 resonance inelastic X-ray Scattering (RIXS) spectra; (D) expanded Ti-L_3 RIXS spectra; (E) Ti 2p and (F) O 1s XPS spectra for $TiO_x(OH)_y$-T_{anneal} and their corresponding fits.

oxygens,[45,46] which have been shown to result in oxygen vacancies.[47] $TiO_x(OH)_y$-RT and $TiO_x(OH)_y$-200 were found to contain trace amounts of chlorine (Figure S5A). The progressive loss of nitrogen along with other moieties, such as surface hydroxyls upon annealing (vide supra), likely induces an atomic rearrangement and densification, leading to more ordered domains.

An additional cause of local disorder in these materials is the presence of Ti^{3+} in the $TiO_x(OH)_y$ matrix. To ascertain the presence and distribution of such species, the $TiO_x(OH)_y$-T_{anneal} samples were further characterized by RIXS. The bulk-sensitive Ti-L_3 RIXS spectra showed features near the elastic line ranging from ~455−457.5 eV of emission energy, which typically correspond to non-d^0 Ti-species in the bulk of the $TiO_x(OH)_y$-RT (Figure 3C). The weak intensity of the detected species suggests that the material is predominantly composed of Ti^{4+}, with only a minor presence of Ti^{3+}. The observed decrease in the bulk Ti^{3+} concentration as the synthesis temperature increases (Figure 3D) correlates with the corresponding decrease of disorder with T_{anneal} in $TiO_x(OH)_y$-T_{anneal}. Interestingly, the Ti 2p XPS (Figure 3E) of $TiO_x(OH)_y$-RT predominantly contained features at BE values of 458.70 and 464.42 eV corresponding to Ti^{4+}, with minor contributions to the intensity from Ti^{3+} species centered at BE values of 457.50 and 462.60 eV.[48] Therefore, upon progressive annealing, the bulk becomes enriched in Ti^{4+} (d^0) relative to Ti^{3+} as evidenced by the Ti-L_3 RIXS.

The XPS results, on the other hand, showed an enhanced contribution from Ti^{3+} species on the surface directly correlating with T_{anneal}. The Ti^{3+}/Ti^{4+} ratio as determined by XPS was found to increase between those of $TiO_x(OH)_y$-RT and $TiO_x(OH)_y$-600 (Figure S5B). The distribution of Ti^{3+}/Ti^{4+} as observed from XPS and RIXS could be rationalized by the synthesis protocol which relies on the aerial oxidation and hydrolysis of a Ti^{3+} precursor. Faster hydrolysis relative to aerial oxidation likely leads to some trapped Ti^{3+} in the bulk of the precipitating $TiO_x(OH)_y$-RT particles. Upon annealing, the Ti^{3+} species in the bulk were found to convert fully to Ti^{4+}, as evidenced from Ti-L_3 RIXS. The increase in surface-confined Ti^{3+} upon annealing as observed by XPS is likely caused by the reduction of surface Ti^{4+} groups during the progressive release of N-species with T_{anneal} (vide supra). The presence of Ti^{3+} was further corroborated by EPR measurements of $TiO_x(OH)_y$-T_{anneal} samples (Figure S5C), where a signal corresponding to a g-value of 1.98 was observed, progressively increasing in intensity with T_{anneal}, in agreement with the XPS data.[49]

The O 1s XPS data of the $TiO_x(OH)_y$-T_{anneal} samples (Figure 3F) indicated contributions from Ti−O−Ti linkages (~529.92 eV and ~528.50 eV), Ti−OH species (~531.00 eV), adsorbed water on the oxygen-deficient regions occurring at higher BEs (~532.50 eV), and adsorbed OH groups (~531.50 eV).[50−55] The O 1s XPS fits pointed to a progressive loss of the Ti−OH groups and oxygen-deficient regions with an increase in T_{anneal}. A concomitant shift to lower BE for the Ti−O−Ti moiety was also observed, particularly for the $TiO_x(OH)_y$-400 and $TiO_x(OH)_y$-600 samples, supporting an increasing presence of Ti^{3+} on the surface at high T_{anneal} (vide supra). An enhanced intensity of the adsorbed OH component in $TiO_x(OH)_y$-600 likely includes contributions from weakly held Ti−OH groups, the amount of which was below the detection limit of the XRD (vide supra). This observation further augmented the existence of some residual disorder in the $TiO_x(OH)_y$-600 sample. The detailed material characterization results, therefore, demonstrated that the controlled annealing in these titanium oxyhydroxide precursors facilitates tuning of material disorder and porosity, which in turn can influence sodium ion storage (vide infra).

2.2. Electrochemical Studies

The electrochemical performance of the different $TiO_x(OH)_y$-T_{anneal} samples were first evaluated under galvanostatic charge/discharge (GCD) cycling conditions in a half-cell configuration against a sodium metal counter electrode at a current density of 260 mA/g between 3 V and 10 mV vs $Na^{+/0}$. Assuming a theoretical specific capacity of 260 mAh/g for insertion of sodium into TiO_2, the applied current density corresponds to a

https://doi.org/10.1021/acs.chemmater.6c00507
Chem. Mater. XXXX, XXX, XXX−XXX

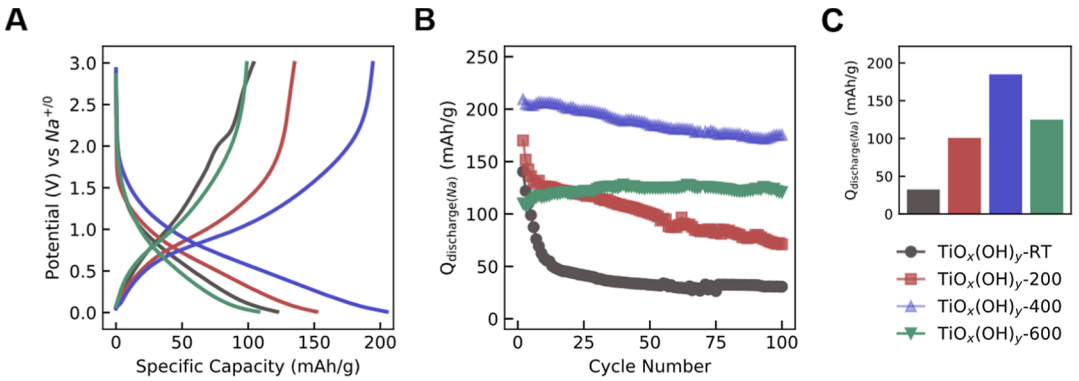

Figure 4. (A) Representative GCD profiles for $TiO_x(OH)_y$-T_{anneal} nanoparticles at 260 mA/g cycled between 0.01 and 3 V vs $Na^{+/0}$ (3rd cycle); (B) specific capacity versus cycle number (2nd cycle onwards); (C) discharge capacities at the 50th cycle for $TiO_x(OH)_y$-T_{anneal}.

1 C rate. At this rate, the GCD profiles for all of the $TiO_x(OH)_y$-T_{anneal} (Figures 4A and S6A) materials showed a sloping voltage profile, lacking any discernible low voltage plateau across several charge−discharge cycles. Owing to their nanoscale dimensions, all the four $TiO_x(OH)_y$-T_{anneal} variants exhibited low Coulombic efficiencies in the first cycle, which, however, quickly recovered and stabilized in the subsequent cycles (Figure S6B). In terms of cycling performance, the moderately disordered $TiO_x(OH)_y$-400 surpassed all of the other variants (refer Table 3) with an average discharge capacity ($Q_{discharge(Na)}$) of ∼188 mAh/g for over 100 charge−discharge cycles with good cycling stability (Figure 4B,C). Given the larger surface area of $TiO_x(OH)_y$-400 compared to that of $TiO_x(OH)_y$-600 (Table 2), capacity fading in the initial cycles is observed, which eventually stabilizes. The observed nonmonotonic trend of specific capacity as a function of particle size with $TiO_x(OH)_y$-T_{anneal} deviates from the strict inverse particle size dependence of the specific capacity in case of purely crystalline TiO_2.[16] The synthetically induced disorder, therefore, likely enables optimal rate performance in $TiO_x(OH)_y$-400 up to a rate of 1.3 A/g or 5 C (Figure S6C).

Table 3. Sodium Storage Performance of Different $TiO_x(OH)_y$-T_{anneal} Materials at 260 mA/g

S. No.	sample	average $Q_{discharge(Na)}$ (mAh/g)
1	$TiO_x(OH)_y$-RT	40.2
2	$TiO_x(OH)_y$-200	101.2
3	$TiO_x(OH)_y$-400	187.8
4	$TiO_x(OH)_y$-600	122.8

To further elucidate the role of disorder in influencing the mechanism of Na^+ storage in these materials, CV experiments were conducted. The CV curves after IR compensation for all the $TiO_x(OH)_y$-T_{anneal} materials except the TiO_x $(OH)_y$-RT showed prominent redox features with an $E_{1/2}$ of 0.73−0.76 V vs $Na^{+/0}$ at a scan rate of 0.1 mV/s, assigned to $Ti^{4+/3+}$ redox (Figure 5A). The broadness of the CV observed in case of TiO_x $(OH)_y$-RT or the smearing of the $Ti^{4+/3+}$ redox potentials across a wider potential window likely stemmed from the presence of disordered domains, resulting in a distribution of chemical environments.[56] To elucidate the mode of Na^+ storage in $TiO_x(OH)_y$-T_{anneal}, the peak current from the CV data obtained at different scan-rates after IR compensation (Figure S7) for each $TiO_x(OH)_y$-T_{anneal} was fitted to the scan-rate according to eq 1.[57] The electrode loadings were reduced to 0.3−0.7 mg/cm^2 for these measurements to minimize the effect of transport resistance in the porous electrode and ensure semi-infinite diffusion dominates the current response.[58]

$$i = a\nu^b \tag{1}$$

In such cases, b = 1 would denote a purely capacitive, surface-confined mode of Na^+ storage, whereas b = 0.5 would denote a diffusive, faradaic process involving Na^+ insertion into the bulk of these electrode materials.[16] From the scan-rate dependent cyclic voltammograms, the "b" values determined for the

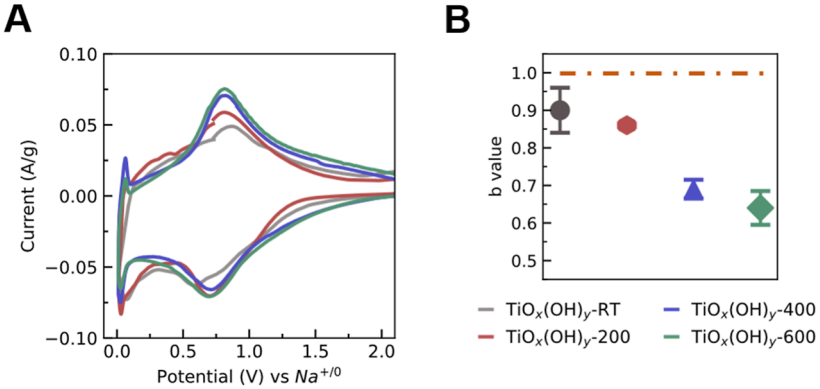

Figure 5. (A) CV plots (smoothened) for $TiO_x(OH)_y$-T_{anneal} at 0.1 mV/s scan rates. (B) Variation in the "b value" for the different $TiO_x(OH)_y$-T_{anneal} samples.

https://doi.org/10.1021/acs.chemmater.6c00507
Chem. Mater. XXXX, XXX, XXX−XXX

$TiO_x(OH)_y$-RT and $TiO_x(OH)_y$-200 samples were found to be around 0.85−0.90, whereas the corresponding values for $TiO_x(OH)_y$-400 and $TiO_x(OH)_y$-600 were found to be between 0.60 and 0.70 (Figure 5B). Hence, in case of the smaller $TiO_x(OH)_y$-T_{anneal} samples, the higher "*b*" value suggests a surface-confined Na^+ storage mechanism, while in the larger $TiO_x(OH)_y$-T_{anneal} samples, a mechanism involving sodiation in the bulk of the particles is likely operative. The "*b*" values determined herein are in contrast to those observed in the case of fully crystalline anatase TiO_2 nanoparticles, wherein the "*b*" value is close to 1 irrespective of the particle size ranging from 1 to 100 nm.[16] The difference in "*b*" values, therefore, suggests that the inherent structural disorder in the $TiO_x(OH)_y$-T_{anneal} class of materials and resulting internal porosity facilitate the movement of the sodium ions into the bulk of the material. This intrinsic porosity scales inversely with T_{anneal} (vide supra), reaching an optimal value at $TiO_x(OH)_y$-400 unlocking superior high-rate sodium ion storage properties (vide infra). Therefore, the temperature-dependent material disorder in Ti-oxyhydroxides ($TiO_x(OH)_y$-T_{anneal}) induced by our synthesis protocol leads to the breaking of the inverse scaling relationship between particle size and $Q_{discharge(Na)}$ that is observed in the case of fully crystalline TiO_2 particles.[16] The breaking of this inverse correlation resulted in the highest $Q_{discharge(Na)}$ and cycling stability at elevated rates in case of $TiO_x(OH)_y$-400, the material with intermediary size, porosity, and disorder in the series of materials prepared herein.

Upon examining the $TiO_x(OH)_y$-400 and $TiO_x(OH)_y$-600 electrodes ex-situ with pXRD after a few sodiation/desodiation cycles at 260 mA/g, broadening was observed, which indicated the growth of disordered domains with Na cycling (Figure S8A,B). To further probe $TiO_x(OH)_y$-400's evolution during cycling, in situ Raman spectra were collected for $TiO_x(OH)_y$-400 at different states-of-sodiation during the first cycle in a specially designed coin cell (Figure S8C,D, see Experimental Section). The initially observed Raman features around 144, 399, 514, and 636 cm^{-1}, corresponding to the E_g, B_{1g}, A_{1g}/B_{1g}, and E_g vibrational modes of anatase TiO_2,[59,60] respectively, were found to progressively weaken and eventually disappear with increasing extent of sodiation. Further, during the subsequent desodiation cycle, these peaks were not found to reappear, thus pointing to irreversible structural changes during the first sodiation.[26,61] Also, no new features were observed to appear in the Raman spectra, which negate the possibility of formation of new phases plausibly linked to the water content and proton-related redox in these materials.[62−64] The former was determined from the TGA data (Figure 1D), assuming that only water loss contributed to the observed mass loss in TGA, which would correspond to an upper bound. Given the low amount of residual water in $TiO_x(OH)_y$-400 (Table S1), which also scales inversely with T_{anneal}, we posit that it is unlikely to be correlated to the structural changes observed herein, even though irreversible loss of protons from water/OH type moieties is expected at these low potentials. Therefore, the local disorder induced from synthesis in $TiO_x(OH)_y$-400 is likely responsible for its superior high-rate Na-storage. To measure the kinetic threshold below which, the synthetically induced disorder would be disrupted, the $TiO_x(OH)_y$-400 samples were subjected to a modified cycling protocol with five initial sodiation/desodiation cycles at 13 mA/g, which corresponds to a slow rate of 0.05 C. Indeed, it was observed that upon subsequent high-rate cycling at 260 mA/g, there was a drop in specific capacity in $TiO_x(OH)_y$-400 (Figure S9).

2.3. Computational Studies

To evaluate the impact of amorphization on sodium intercalation capacity in silico, melt-quench simulations using ab initio molecular dynamics (AIMD)[65] were conducted on dihydrogen trioxotitanate ($TiO(OH)_2$, ICSD database code 195648)[66] to obtain amorphous $TiO(OH)_2$. Initially, potential ordered structural arrangements corresponding to the disordered $TiO(OH)_2$ structure found in the ICSD were enumerated. Subsequently, density functional theory (DFT) calculations were performed on the enumerated structures to identify the ground-state ordered structure. The Hubbard *U* corrected strongly constrained and appropriately normed (SCAN) functional was used for the DFT calculations to identify the ground-state of $TiO(OH)_2$, applying a *U* value of 2.5 eV to Ti atoms to accurately represent on-site Coulombic interactions.[67−70] To minimize computational costs, all DFT/AIMD calculations were performed on $TiO(OH)_2$ starting from its primitive cell as obtained in the ICSD.

The resulting DFT-calculated ground-state structure was heated incrementally from 0 to 2000 K using a time step of 2 fs over a total duration of 10 ps. The maximum temperature was chosen as 2000 K in our heating step since this is approximately the melting point of titanium, the element with the highest melting point in our system. To ensure proper equilibration of $TiO(OH)_2$ at 2000 K, the structure was maintained at 2000 K for an additional 10 ps after the heating step. Subsequently, the structure was quenched to lower temperatures in a stepwise manner, specifically, 1500, 1000, 600, and 300 K, at a cooling rate of 250 K/ps. Each quenching process involved cooling the structure to the targeted temperature at a time step of 2 fs, followed by equilibration at the target temperature for an additional 2 ps. To circumvent computational convergence issues caused by hydrogen atoms, the initial melt-quench simulations were performed using the generalized gradient approximation (GGA)[71] without hydrogen atoms. Once equilibrium at the targeted quenching temperature was achieved, hydrogen atoms were manually reintroduced into the structure.

To identify potential locations for sodium ion intercalation in $TiO(OH)_2$ after the melt-quench simulations, the Voronoi polyhedra construction method was used, as implemented in the Topography Analyzer class of the pymatgen[72] library, and constructed a Voronoi polyhedron for each atom within the structure. Note that the Voronoi polyhedron, which is an envelope of planes around an atom of interest, represents the region in space that is closer to the atom of interest than any other atom in the structure. The vertices of these polyhedra define potential void spaces within the material that might accommodate intercalating (or interstitial) ions, signifying possible sites that Na^+ can occupy within the $TiO(OH)_2$ structure. Furthermore, to assess the stability of Na^+ in these Voronoi-identified voids, the Ewald site energy of each possible nonoverlapping site was calculated using the Ewald Summation class in pymatgen. The Ewald method efficiently computes the long-range electrostatic (Coulombic) energy within crystal lattices by partitioning the calculations into a direct-space sum, and a reciprocal-space sum, accounting for short and long-range interactions, respectively. By combining these two terms, the total Coulombic energy of potential Na sites is accurately determined. Finally, the Voronoi-identified sites with a

https://doi.org/10.1021/acs.chemmater.6c00507
Chem. Mater. XXXX, XXX, XXX−XXX

negative Ewald energy (or negative electrostatic energy) were considered as possible or stable sites for Na^+ occupation within $TiO(OH)_2$. A count of the available intercalation sites per formula unit is displayed in Table 4.

Table 4. Number of Na^+ Intercalation Sites for Structures Obtained at Different Quenching Temperatures from the AIMD Simulations

temperature (K)	no. of Na sites per formula unit
1500	0
1000	1.5
600	1
300	1

Pair-distribution functions (PDFs) were calculated to characterize the atomic ordering and structural arrangement of equilibrated structures, with potential Na intercalation sites, at quenching temperatures of 1500, 1000, 600, and 300 K, and have illustrated the calculated PDFs in Figure 6b–e. The PDF for the ground-state ordered $TiO(OH)_2$ structure (i.e., the crystalline structure) is shown in Figure 6a, while Figure 6f depicts an equilibrated structure at 300 K containing Na^+ ions occupying identified void spaces. Blue, green, black, and red lines in Figure 6a–e represent Ti–Ti, O–O, Ti–O, and Na–O pairs, respectively. Note that there are no Na–O pairs for the $TiO(OH)_2$ structure quenched to 1500 K (Figure 6b) since we do not identify any stable Na^+ sites using our electrostatic energy calculations (Table 4).

In crystalline materials, PDFs exhibit sharp, well-defined peaks corresponding to specific interatomic distances, which is consistent with our observation in Figure 6a, with sharp peaks up to 5 Å. Conversely, amorphous materials show broader, less distinct features, as highlighted by the reduced peak intensities and increase in the width of all peaks in Figure 6b–e compared to Figure 6a. Notably, structures quenched to higher temperatures (e.g., 1500 and 1000 K) exhibit higher degrees of amorphization in our simulations than lower quenched temperatures (e.g., 600 and 300 K), as characterized by sharper and narrower peaks for Ti–O and Na–O bonds in the 300 and 600 K structures compared to 1000 K. Thus, the simulated structures become more crystalline with lower quenching temperatures, which can be attributed to higher availability of thermal energy at higher simulation temperatures.

Interestingly, our simulated data on crystallinity (Figure 6a–e), which show increasing crystallinity with lower quenched temperatures, are seemingly in contrast with our pXRD observations (Figure 1), which indicate an increase in crystallinity with higher annealing temperatures. However, our experimental synthesis traps the metastable amorphous structure already at room temperature unlike our simulations, which are designed to get the ground-state structure at all temperatures. Subsequently, as higher thermal energy is provided to the system experimentally, it transforms more

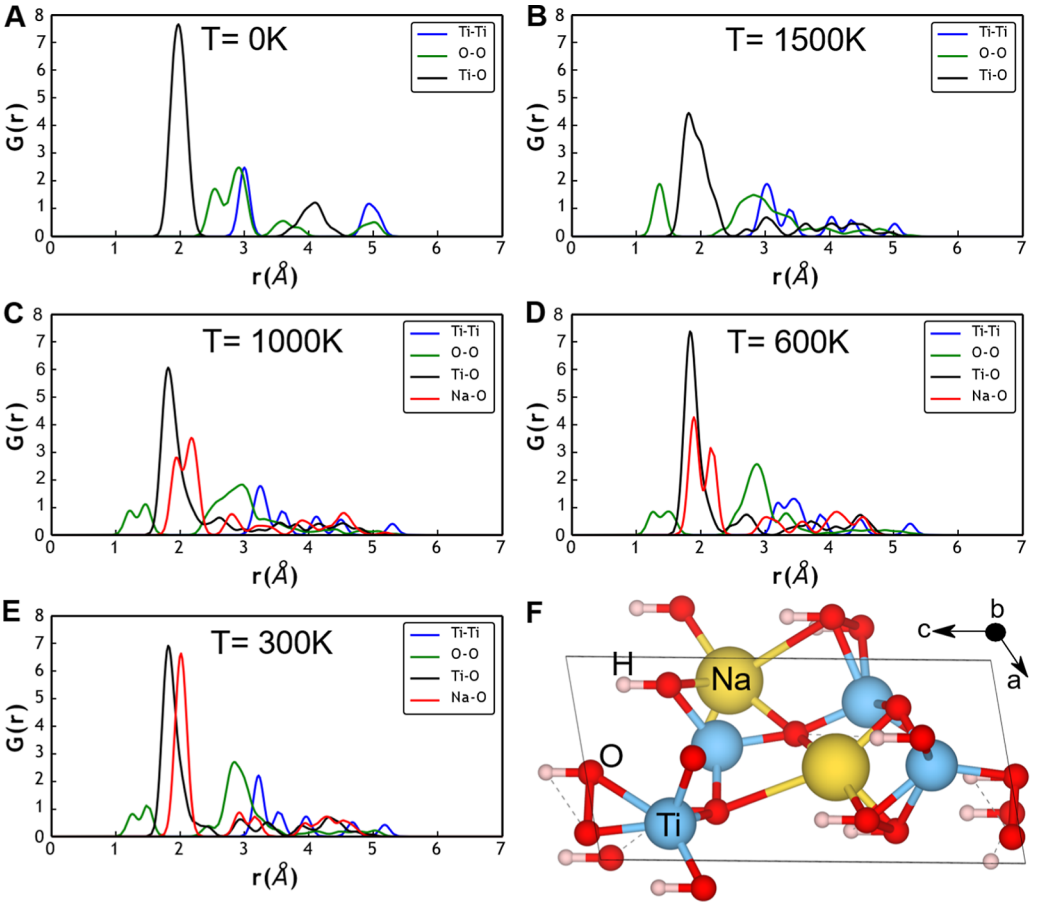

Figure 6. PDFs of the (A) ground-state $TiO(OH)_2$ structure, and structures quenched to (B) 1500 K, (C) 1000 K, (D) 600 K, and (E) 300 K in our AIMD simulations. (F) Structure quenched to 300 K with the potential voids occupied by Na^+. Yellow, blue, red, and pink spheres indicate Na, Ti, O, and H, respectively.

https://doi.org/10.1021/acs.chemmater.6c00507
Chem. Mater. XXXX, XXX, XXX–XXX

readily to the thermodynamically stable crystalline structure while our melt-quench simulations attempt to trap the metastable amorphous configuration and prevent it from becoming fully crystalline. Thus, our simulation temperatures cannot be compared directly with experimental temperatures, but the degree of amorphization/crystallinity obtained during simulations can be compared directly with experimental observations.

Importantly, our AIMD data indicate that the intermediate quenched temperature of 1000 K (or structure with an intermediate degree of amorphization, Figure 6c) exhibits the highest number of Na^+ sites that can be occupied (Table 4). In other words, when $TiO(OH)_2$ becomes fully amorphous (at 1500 K, Figure 6b) or closer to the crystalline structure (at 300 K, Figure 6e), the number of possible Na^+ sites drops compared to the structure with an intermediate degree of amorphization (at 1000 K), signifying that the Na^+ intercalation capacity should exhibit a nonmonotonic variation with the degree of amorphization of $TiO(OH)_2$, and structures with an intermediate degree of amorphization should display higher capacities. This computational observation on the available Na^+ sites with a degree of amorphization aligns with our electrochemical GCD experiments (Figure 4) that demonstrate moderately disordered (or amorphous) $TiO_x(OH)_y$-400 materials exhibiting a higher discharge capacity than fully disordered or fully crystalline. Thus, the degree of amorphization in $TiO(OH)_2$ is an important factor that governs its electrochemical properties and requires careful optimization.

3. CONCLUSIONS

In a series of titanium oxyhydroxide materials ($TiO_x(OH)_y$-T_{anneal}), the role of material disorder induced from the synthetic protocol in unlocking high Na^+ storage capacity at elevated rates has been demonstrated. These materials were synthesized via a scalable, solution-phase approach employing a Ti(III) precursor, resulting in a systematic modulation of disorder as a function of T_{anneal} through the incorporation of interstitial N atoms, O-vacancies, and Ti(III) sites. $TiO_x(OH)_y$-400, with an intermediary size and extent of disorder in the series of materials reported herein, showed the highest specific capacity (~188 mAh/g) and cycling stability during Na-storage at an elevated current density of 260 mA/g. Our experimental observations are in line with our computational data, which show a higher number of possible sites that Na^+ can occupy with an intermediate level of disorder in a $TiO(OH)_2$ composition. Further, the presence of disorder was found to break the inverse scaling between size and specific capacity observed in the case of fully crystalline anatase TiO_2, resulting in a diffusion-driven bulk Na-storage mechanism, posited to lead to higher specific capacity even for larger particle sizes. The results inform material design strategies to unlock high specific capacity and cycling stability at elevated rates despite Na-insertion-induced amorphization via the incorporation of specific amounts of disorder through scalable synthetic approaches.

4. EXPERIMENTAL SECTION

4.1. Material Synthesis

4.1.1. Synthesis of $TiO_x(OH)_y$-T_{anneal}. 5 mL of the $TiCl_3$ solution (15% $TiCl_3$ in 10% HCl, Sigma-Aldrich) was added to 100 mL of DI water and stirred at room temperature. To this solution, 400 mL of aqueous ammonia (13.4 N) was added dropwise under constant stirring until the formation of a deep blue precipitate. This solution was stirred under ambient conditions for another 120 min during which the blue precipitate turned white. The white precipitate was subsequently filtered under vacuum and dried at 80 °C in air. The Ti^{3+}/NH_3 molar ratio was maintained above 0.7 during the first step of the synthesis. The as-obtained $TiO_x(OH)_y$ -RT was heated in a muffle furnace (AntsLab) in air at 200, 400, and 600 °C for 4 h to obtain the annealed series of $TiO_x(OH)_y$-T_{anneal} materials.

4.2. Sample Characterization

The $TiO_x(OH)_y$-T_{anneal} samples were first characterized by using pXRD at room temperature on a Rigaku Smart Lab SE diffractometer using Cu Kα radiation (λ = 1.5419 Å) to confirm phase purity. Rietveld refinement of the powder XRD patterns was performed using Profex (version 4.3.3) software.[73] The diffraction patterns were refined using an anatase (TiO_2) structural model and the following parameters was varied during the refinement: unit cell constants, crystallite size parameter (B1), Ti site occupancy, and thermal displacement parameters of Ti and O (B_{iso} in nm^2).[74] FTIR spectra were recorded on a Spectrum One IR spectrophotometer (PerkinElmer) fitted with a KBr pellet setup. The spectra were recorded in the range 4000−400 cm^{-1} after finely grinding the samples with KBr and pressing them into pellets. The thermogravimetric analysis (TGA) for these materials was performed using a thermo gravimetric mass analyzer (Rigaku Corporation) under N_2 at a constant heating rate of 10 °C/min. The morphology of the materials was analyzed using transmission electron microscopy (Themis 300 G3 TEM, Thermo Scientific) at 300 kV fitted with a scintillator-based CETA-D camera (Thermo Scientific). The samples for TEM were prepared by dispersing $TiO_x(OH)_y$-T_{anneal} powders in ethanol and drop casting them on to Cu-coated 200 mesh grids. The elemental analyses for the $TiO_x(OH)_y$-T_{anneal} samples were recorded on a Thermos Finnigan (FLASH EA 1112 series) microanalyzer. The surface chemical composition of $TiO_x(OH)_y$-T_{anneal} was determined by XPS (Kratos Analytical Axis Supra, monochromatic Al Kα X-ray source, 1486.6 eV). The XPS least-squares fittings were performed using CASA software, ensuring the chemical environments were fitted within the range of ±0.5 eV and the fwhm constrained between 1.0−2.5 eV applying a Shirley background. The Ti-L_3 RIXS spectra were collected at beamline 8.0.1.1 at Advanced Light Source in Lawrence Berkeley National Laboratory. The samples for Ti-L_3 RIXS measurement were prepared in a N_2-filled glovebox. All Ti-L_3 RIXS spectra were collected at 457.7 eV, which is the Ti-L_3 t_{2g} resonance of TiO_2. The EPR data were collected on a JEOL FA200 X-band (9.5 GHz) ESR spectrometer at 25 °C. N_2 adsorption/desorption was measured on an Autosorb IQ BET Surface Area Analyzer (Anton Paar), after degassing under vacuum at 130 °C for 12 h.

4.3. Preparation of Electrodes and Cell Fabrication

The electrode slurries were prepared by mixing the active material ($TiO_x(OH)_y$-T_{anneal}) with carbon black (MTI Corp, stored in a vacuum oven at 60 °C) and polyvinylidene fluoride (PVDF) (Arkema) binder in an 80:10:10 ratio by weight in *N*-methylpyrrolidinone (NMP, Sigma-Aldrich). The mixture was thoroughly homogenized at progressively increasing rotation rates (500 to 2000 rpm) using a planetary mixer (Thinky Corp.) for ~10 min. The resulting slurries were then tape-cast onto a battery grade 12 μm thick copper foil (Gelon Lib Group Co.) using a blade coater (MTI Corp.) followed by drying under vacuum at 60 °C for 12 h. The dried slurry was subsequently calendared (MTI Corp.) to a final thickness of ~120 μm followed by punching into 14 mm discs. The resultant active material loading in the case of the $TiO_x(OH)_y$-T_{anneal} materials was in the range of 1.3−2.6 mg/cm^2. CR2032 coin cells (MTI Corp.) were assembled in an Ar-filled glovebox (Jacomex, H_2O < 0.1 ppm; O_2 < 1 ppm) with the $TiO_x(OH)_y$-T_{anneal} working electrodes against a Na foil (Sigma-Aldrich) counter electrode. A Whatman GF/D filter paper (~800 μm thickness) was used as the separator; 180 μL of 1 M $NaBF_4$ (Sigma-Aldrich) in tetraethylene glycol dimethyl ether (or Tetraglyme, Sigma-Aldrich) was used as the electrolyte. For the in situ Raman measurements, carbon-free electrodes were prepared by

https://doi.org/10.1021/acs.chemmater.6c00507
Chem. Mater. XXXX, XXX, XXX−XXX

mixing $TiO_x(OH)_y$-400 with PVDF (Arkema) binder in an 90:10 ratio by weight in NMP, followed by coating on a battery grade 12 μm thick copper foil (Gelon Lib Group Co.) with a wet thickness of ∼40 μm. After being dried, the coatings were punched into 11 mm discs. For the ex-situ pXRD measurements, the $TiO_x(OH)_y$-T_{anneal} electrodes were extracted after carefully decrimping the coin cells in the charged (desodiated) state inside the argon-filled glovebox. They were subsequently rinsed with dimethyl carbonate (Sigma-Aldrich), dried, and transferred to the X-ray diffractometer.

4.4. Electrochemical Studies

Long-term galvanostatic charge−discharge experiments on the $TiO_x(OH)_y$-T_{anneal} materials were performed using a multichannel BTS 4000 battery cycler (Neware Technology Limited). The fabricated coin cells were kept at rest for 16 h prior to cycling. The charge−discharge experiments were performed using a constant-current (CC) protocol within a voltage window of 0.01−3.00 V vs $Na^{+/0}$. CV scans were performed using a Biologic BCS 805 cycler (Biologic Instruments) at scan rates of 0.1 mV/s, 0.25 mV/s, 0.5 mV/s, and 1 mV/s between 0.01 and 3.00 V. The voltammograms were smoothened using the Savitzky−Golay method using a polynomial order of 2 and window size of 200 points. For the *b*-value calculations, the peak currents were obtained from IR-corrected voltammograms (Figure S7). The in situ Raman experiments were performed with the help of a Raman spectrometer (inVia Reflex model, Renishaw, UK) with 532 nm laser source. A customized coin cell with a perforated cap and a spacer with a hole was employed. A separator (16 mm in diameter) and Na metal foil (13 mm in diameter), with aligned holes in the center, were used to allow the laser to reach the sample (Figure S8C). The perforation on the cap was sealed with a Kapton tape during cell assembly inside the argon-filled glovebox. The potential of the cell was controlled by an SP-150e potentiostat (Biologic Instruments).

4.5. Computational Details

AIMD simulations were performed using the Vienna Ab initio Simulation Package VASP, version 6.1.2.[75,76] The projector augmented wave[77] method was employed to represent the frozen core electrons, and a plane-wave basis set with a kinetic energy cutoff of 520 eV was used to expand the one-electron wave functions. To obtain the ground-state structure of $TiO(OH)_2$ from the enumerated structures, the electronic exchange and correlation were modeled using the SCAN + *U meta*-GGA functional, while GGA was used for the melt-quench simulations due to convergence difficulties after removing the H atoms. A cooling rate of 250 K/ps was fixed during quenching. The convergence threshold for the total energy and atomic forces was set to 0.01 meV and |0.01| eV per Å, respectively. The Brillouin zone was sampled using Γ-centered Monkhorst−Pack *k*-point meshes with a density of at least 48 *k*-points per unit reciprocal space vector.

■ ASSOCIATED CONTENT

Supporting Information

The Supporting Information is available free of charge at https://pubs.acs.org/doi/10.1021/acs.chemmater.6c00507.

Characterization data (Rietveld refinement, BET adsorption isotherms, and EPR) along with electrochemical data (PDF)

■ AUTHOR INFORMATION

Corresponding Author

Srinivasan Ramakrishnan − *Department of Chemistry, Indian Institute of Technology Bombay, Mumbai 400076, India;* orcid.org/0000-0003-3204-8095; Phone: +91-22-2576-7197; Email: srini@chem.iitb.ac.in

Authors

Dnyanesh Vernekar − *Department of Chemistry, Indian Institute of Technology Bombay, Mumbai 400076, India;* orcid.org/0000-0002-1540-7466

Soumyajit Gupta − *Department of Chemistry, Indian Institute of Technology Bombay, Mumbai 400076, India*

Gi-Hyeok Lee − *Advanced Light Source, Lawrence Berkeley National Laboratory, Berkeley, California 94720, United States*

Reshma Devi − *Department of Materials Engineering, Indian Institute of Science, Bengaluru 560012, India*

Mohamed Ruwaid Rafiuddin − *MIAMI Facility, School of Computing and Engineering, University of Huddersfield, Huddersfield HD1 3DH, U.K.;* orcid.org/0000-0002-0190-1092

Gopalakrishnan Sai Gautam − *Department of Materials Engineering, Indian Institute of Science, Bengaluru 560012, India;* orcid.org/0000-0002-1303-0976

Wanli Yang − *Advanced Light Source, Lawrence Berkeley National Laboratory, Berkeley, California 94720, United States;* orcid.org/0000-0003-0666-8063

Complete contact information is available at: https://pubs.acs.org/10.1021/acs.chemmater.6c00507

Author Contributions

⊥D.V. and S.G. contributed equally.

Notes

The authors declare no competing financial interest.

■ ACKNOWLEDGMENTS

S.R. acknowledges research funding from the Board of Research on Nuclear Sciences, Government of India (sanction number 58/20/13/2024-BRNS) and an international travel grant through the Institute of Eminence Cell at IIT Bombay (R.D./0523-IOE00I0-108). D.V. is grateful to IIT Bombay for an Institute Postdoctoral Fellowship, S.G. is grateful to the CSIR, Government of India, for a graduate fellowship. S.R., D.V., and S.G. acknowledge the Department of Chemistry and Sophisticated Analytical Instrumentation Facility at IIT Bombay for access to characterization facilities and thank Prof. C. Subramaniam and Dr. Mohammed Aslam Villan for their inputs on the in situ Raman spectroscopy measurements. G.S.G. acknowledges financial support from the Science and Engineering Research Board (SERB) of the Department of Science and Technology, Government of India, under sanction number IPA/2021/000007. R.D. thanks the Ministry of Human Resource Development, Government of India, for financial assistance. R.D. and G.S.G. acknowledge the computational resources provided by the Supercomputer Education and Research Centre, IISc, for enabling some of the calculations showcased in this work. Soft X-ray spectroscopy and data processing used resources of the Advanced Light Source, which is a DOE Office of Science User Facility under contract number DE-AC02-05CH11231.

■ REFERENCES

(1) Gür, T. M. Review of Electrical Energy Storage Technologies, Materials and Systems: Challenges and Prospects for Large-Scale Grid Storage. *Energy Environ. Sci.* **2018**, *11* (10), 2696−2767.

(2) Vaalma, C.; Buchholz, D.; Weil, M.; Passerini, S. A Cost and Resource Analysis of Sodium-Ion Batteries. *Nat. Rev. Mater.* **2018**, *3* (4), 18013.

(3) Abraham, K. M. How Comparable Are Sodium-Ion Batteries to Lithium-Ion Counterparts? *ACS Energy Lett.* **2020**, *5* (11), 3544−3547.
(4) Kubota, K.; Komaba, S. Review—Practical Issues and Future Perspective for Na-Ion Batteries. *J. Electrochem. Soc.* **2015**, *162* (14), A2538−A2550.
(5) Mogensen, R.; Brandell, D.; Younesi, R. Solubility of the Solid Electrolyte Interphase (SEI) in Sodium Ion Batteries. *ACS Energy Lett.* **2016**, *1* (6), 1173−1178.
(6) Moriwake, H.; Kuwabara, A.; Fisher, C. A. J.; Ikuhara, Y. Why Is Sodium-Intercalated Graphite Unstable? *RSC Adv.* **2017**, *7* (58), 36550−36554.
(7) Liu, Y.; Merinov, B. V.; Goddard, W. A. Origin of Low Sodium Capacity in Graphite and Generally Weak Substrate Binding of Na and Mg among Alkali and Alkaline Earth Metals. *Proc. Natl. Acad. Sci. U.S.A.* **2016**, *113* (14), 3735−3739.
(8) Irisarri, E.; Ponrouch, A.; Palacin, M. R. Review—Hard Carbon Negative Electrode Materials for Sodium-Ion Batteries. *J. Electrochem. Soc.* **2015**, *162* (14), A2476−A2482.
(9) Stevens, D. A.; Dahn, J. R. High Capacity Anode Materials for Rechargeable Sodium-Ion Batteries. *J. Electrochem. Soc.* **2000**, *147* (4), 1271.
(10) Zhang, B.; Ghimbeu, C. M.; Laberty, C.; Vix-Guterl, C.; Tarascon, J. M. Correlation between Microstructure and Na Storage Behavior in Hard Carbon. *Adv. Energy Mater.* **2016**, *6* (1), 1−9.
(11) Bommier, C.; Surta, T. W.; Dolgos, M.; Ji, X. New Mechanistic Insights on Na-Ion Storage in Nongraphitizable Carbon. *Nano Lett.* **2015**, *15* (9), 5888−5892.
(12) Tahir, M. N.; Oschmann, B.; Buchholz, D.; Dou, X.; Lieberwirth, I.; Panthöfer, M.; Tremel, W.; Zentel, R.; Passerini, S. Extraordinary Performance of Carbon-Coated Anatase TiO2 as Sodium-Ion Anode. *Adv. Energy Mater.* **2016**, *6* (4), 1501489.
(13) Patra, J.; Wu, S. C.; Leu, I. C.; Yang, C. C.; Dhaka, R. S.; Okada, S.; Yeh, H. L.; Hsieh, C. M.; Chang, B. K.; Chang, J. K. Hydrogenated Anatase and Rutile TiO2for Sodium-Ion Battery Anodes. *ACS Appl. Energy Mater.* **2021**, *4* (6), 5738−5746.
(14) Vazquez-Santos, M. B.; Tartaj, P.; Morales, E.; Amarilla, J. M. TiO 2 Nanostructures as Anode Materials for Li/Na-Ion Batteries. *Chem. Rec.* **2018**, *18* (7−8), 1178−1191.
(15) Longoni, G.; Pena Cabrera, R. L.; Polizzi, S.; D'Arienzo, M.; Mari, C. M.; Cui, Y.; Ruffo, R. Shape-Controlled TiO2 Nanocrystals for Na-Ion Battery Electrodes: The Role of Different Exposed Crystal Facets on the Electrochemical Properties. *Nano Lett.* **2017**, *17* (2), 992−1000.
(16) Wei, Q.; Chang, X.; Butts, D.; DeBlock, R.; Lan, K.; Li, J.; Chao, D.; Peng, D. L.; Dunn, B. Surface-Redox Sodium-Ion Storage in Anatase Titanium Oxide. *Nat. Commun.* **2023**, *14* (1), 1−9.
(17) Gentili, V.; Brutti, S.; Hardwick, L. J.; Armstrong, A. R.; Panero, S.; Bruce, P. G. Lithium Insertion into Anatase Nanotubes. *Chem. Mater.* **2012**, *24* (22), 4468−4476.
(18) Kim, K. T.; Ali, G.; Chung, K. Y.; Yoon, C. S.; Yashiro, H.; Sun, Y. K.; Lu, J.; Amine, K.; Myung, S. T. Anatase Titania Nanorods as an Intercalation Anode Material for Rechargeable Sodium Batteries. *Nano Lett.* **2014**, *14* (2), 416−422.
(19) Weppner, W.; Huggins, R. A. Determination of the Kinetic Parameters of Mixed-Conducting Electrodes and Application to the System Li3Sb. *J. Electrochem. Soc.* **1977**, *124* (10), 1569−1578.
(20) Swamy, T.; Chiang, Y.-M. Electrochemical Charge Transfer Reaction Kinetics at the Silicon-Liquid Electrolyte Interface. *J. Electrochem. Soc.* **2015**, *162* (13), A7129−A7134.
(21) Odani, A.; Nimberger, A.; Markovsky, B.; Sominski, E.; Levi, E.; Kumar, V. G.; Motiei, M.; Gedanken, A.; Dan, P.; Aurbach, D. Development and Testing of Nanomaterials for Rechargeable Lithium Batteries. *J. Power Sources* **2003**, *119*−*121*, 517−521.
(22) Kim, N.; Raj, M. R.; Lee, G. Nitrogen-Doped TiO 2 (B) Nanobelts Enabling Enhancement of Electronic Conductivity and Efficiency of Lithium-Ion Storage. *Nanotechnology* **2020**, *31* (41), 415401.
(23) Wang, W.; Liu, Y.; Wu, X.; Wang, J.; Fu, L.; Zhu, Y.; Wu, Y.; Liu, X. Advances of TiO2 as Negative Electrode Materials for Sodium-Ion Batteries. *Adv. Mater. Technol.* **2018**, *3* (9), 1800004.
(24) Cha, H. A.; Jeong, H. M.; Kang, J. K. Nitrogen-Doped Open Pore Channeled Graphene Facilitating Electrochemical Performance of TiO2 Nanoparticles as an Anode Material for Sodium Ion Batteries. *J. Mater. Chem. A* **2014**, *2* (15), 5182−5186.
(25) Xiong, Y.; Qian, J.; Cao, Y.; Ai, X.; Yang, H. Graphene-Supported TiO2 Nanospheres as a High-Capacity and Long-Cycle Life Anode for Sodium Ion Batteries. *J. Mater. Chem. A* **2016**, *4* (29), 11351−11356.
(26) Wu, L.; Bresser, D.; Buchholz, D.; Giffin, G. A.; Castro, C. R.; Ochel, A.; Passerini, S. Unfolding the Mechanism of Sodium Insertion in Anatase TiO2 Nanoparticles. *Adv. Energy Mater.* **2015**, *5* (2), 1401142.
(27) Li, W.; Fukunishi, M.; Morgan, B. J.; Borkiewicz, O. J.; Chapman, K. W.; Pralong, V.; Maignan, A.; Lebedev, O. I.; Ma, J.; Groult, H.; Komaba, S.; Dambournet, D. A Reversible Phase Transition for Sodium Insertion in Anatase TiO2. *Chem. Mater.* **2017**, *29* (4), 1836−1844.
(28) Wagemaker, M.; Mulder, F. M. Properties and Promises of Nanosized Insertion Materials for Li-Ion Batteries. *Acc. Chem. Res.* **2013**, *46* (5), 1206−1215.
(29) Bi, H.; Zhu, S.; Liang, Y.; Jiang, H.; Li, Z.; Wu, S.; Wei, H.; Chang, C.; Wang, H.; Cui, Z. Improved Ions Storage Performance for Various Batteries: Anatase TiO2 with High-Concentration of Ti Vacancies. *Mater. Chem. Phys.* **2023**, *301*, 127591.
(30) Usui, H.; Domi, Y.; Sadamori, Y.; Tanaka, R.; Hoshi, T.; Tanaka, T.; Sakaguchi, H. Nickel-Doped Titanium Oxide with the Rutile Structure for High-Performance Sodium Storage. *ACS Mater. Au* **2025**, *5* (3), 558−568.
(31) Cui, M.; Liu, M.; Li, X.; Shi, W.; Yu, Y.; Li, J.; Liu, Y.; Zhang, F.; Wang, W.; Li, X.; Shao, C.; Liu, Y. Order-Disorder Structural Engineering of Vanadium Oxide Anode: Balancing Ionic and Electronic Dynamic for Fast-Charging Aqueous Li-Ion Battery. *Energy Storage Mater.* **2024**, *70* (February), 103453.
(32) Jiang, H. B.; Cuan, Q.; Wen, C. Z.; Xing, J.; Wu, D.; Gong, X.; Li, C.; Yang, H. G. Anatase TiO 2 Crystals with Exposed High-Index Facets. *Angew. Chem.* **2011**, *123* (16), 3848−3852.
(33) Toorabally, M.; Singh, A.; Sorriaux, M.; Taylor, P. J.; Lantelme, F.; Duttine, M.; Legein, C.; Body, M.; Krins, N.; Bregiroux, D.; Morgan, B. J.; Dambournet, D.; Laberty-Robert, C. Enhanced Cycle Life and Expanded Voltage Window in Aqueous Proton Full Cells Using TiO 2 Negative Electrodes with Cationic Vacancies. *Chem. Mater.* **2024**, *36* (20), 10238−10248.
(34) Grey, I. E.; Wilson, N. C. Titanium Vacancy Defects in Sol-Gel Prepared Anatase. *J. Solid State Chem.* **2007**, *180* (2), 670−678.
(35) Li, Y.; White, T. J.; Lim, S. H. Low-Temperature Synthesis and Microstructural Control of Titania Nano-Particles. *J. Solid State Chem.* **2004**, *177* (4−5), 1372−1381.
(36) Brubach, J.-B.; Mermet, A.; Filabozzi, A.; Gerschel, A.; Roy, P. Signatures of the Hydrogen Bonding in the Infrared Bands of Water. *J. Chem. Phys.* **2005**, *122* (18), 184509.
(37) Bezrodna, T.; Puchkovska, G.; Shymanovska, V.; Baran, J.; Ratajczak, H. IR-Analysis of H-Bonded H2O on the Pure TiO2 Surface. *J. Mol. Struct.* **2004**, *700* (1−3), 175−181.
(38) Abazari, R.; Mahjoub, A. R.; Sanati, S. A Facile and Efficient Preparation of Anatase Titania Nanoparticles in Micelle Nano-reactors: Morphology, Structure, and Their High Photocatalytic Activity under UV Light Illumination. *RSC Adv.* **2014**, *4* (99), 56406−56414.
(39) Dankar, J.; Pagis, C.; Rivallan, M.; El-Roz, M. Operando FTIR Study of the Photocatalytic Reduction of CO2 in the Presence of Water Vapor over Pt/TiO2: On the Role of Surface Residual C-Species. *Sustain. Energy Fuels* **2023**, *7* (12), 2819−2823.
(40) Yin, W.; Barim, G.; Peng, X.; Kedzie, E. A.; Scott, M. C.; McCloskey, B. D.; Doeff, M. M. Tailoring the Structure and Electrochemical Performance of Sodium Titanate Anodes by Post-Synthesis Heating. *J. Mater. Chem. A* **2022**, *10* (47), 25178−25187.

https://doi.org/10.1021/acs.chemmater.6c00507
Chem. Mater. XXXX, XXX, XXX−XXX

(41) Jagadale, T. C.; Takale, S. P.; Sonawane, R. S.; Joshi, H. M.; Patil, S. I.; Kale, B. B.; Ogale, S. B. N-Doped TiO2 Nanoparticle Based Visible Light Photocatalyst by Modified Peroxide Sol-Gel Method. *J. Phys. Chem. C* **2008**, *112* (37), 14595−14602.
(42) Wei, C.; Sun, S.; Mandler, D.; Wang, X.; Qiao, S. Z.; Xu, Z. J. Approaches for Measuring the Surface Areas of Metal Oxide Electrocatalysts for Determining Their Intrinsic Electrocatalytic Activity. *Chem. Soc. Rev.* **2019**, *48* (9), 2518−2534.
(43) Luisa Ojeda, M.; Marcos Esparza, J.; Campero, A.; Cordero, S.; Kornhauser, I.; Rojas, F. On Comparing BJH and NLDFT Pore-Size Distributions Determined from N2 Sorption on SBA-15 Substrata. *Phys. Chem. Chem. Phys.* **2003**, *5* (9), 1859.
(44) Lynch, J.; Giannini, C.; Cooper, J. K.; Loiudice, A.; Sharp, I. D.; Buonsanti, R. Substitutional or Interstitial Site Selective Nitrogen Doping in TiO2 Nanostructures. *J. Phys. Chem. C* **2015**, *119* (13), 7443−7452.
(45) Di Valentin, C.; Finazzi, E.; Pacchioni, G.; Selloni, A.; Livraghi, S.; Paganini, M. C.; Giamello, E. N-Doped TiO2: Theory and Experiment. *Chem. Phys.* **2007**, *339* (1−3), 44−56.
(46) Sathish, M.; Viswanathan, B.; Viswanath, R. P.; Gopinath, C. S. Synthesis, Characterization, Electronic Structure, and Photocatalytic Activity of Nitrogen-Doped TiO2 Nanocatalyst. *Chem. Mater.* **2005**, *17* (25), 6349−6353.
(47) Foo, C.; Li, Y.; Lebedev, K.; Chen, T.; Day, S.; Tang, C.; Tsang, S. C. E. Characterisation of Oxygen Defects and Nitrogen Impurities in TiO2 Photocatalysts Using Variable-Temperature X-Ray Powder Diffraction. *Nat. Commun.* **2021**, *12* (1), 1−13.
(48) Godfroid, T.; Gouttebaron, R.; Dauchot, J. .; Leclère, P.; Lazzaroni, R.; Hecq, M. Growth of Ultrathin Ti Films Deposited on SnO2 by Magnetron Sputtering. *Thin Solid Films* **2003**, *437* (1−2), 57−62.
(49) Kumar, C. P.; Gopal, N. O.; Wang, T. C.; Wong, M.-S.; Ke, S. C. EPR Investigation of TiO 2 Nanoparticles with Temperature-Dependent Properties. *J. Phys. Chem. B* **2006**, *110* (11), 5223−5229.
(50) Dong, F.; Zhao, W.; Wu, Z. Characterization and Photocatalytic Activities of C, N and S Co-Doped TiO2 with 1D Nanostructure Prepared by the Nano-Confinement Effect. *Nanotechnology* **2008**, *19* (36), 365607.
(51) McCafferty, E.; Wightman, J. P. Determination of the Concentration of Surface Hydroxyl Groups on Metal Oxide Films by a Quantitative XPS Method. *Surf. Interface Anal.* **1998**, *26* (8), 549−564.
(52) Sanjinés, R.; Tang, H.; Berger, H.; Gozzo, F.; Margaritondo, G.; Lévy, F. Electronic Structure of Anatase TiO2 Oxide. *J. Appl. Phys.* **1994**, *75* (6), 2945−2951.
(53) Chen, X.; Liu, L.; Yu, P. Y.; Mao, S. S. Increasing Solar Absorption for Photocatalysis with Black Hydrogenated Titanium Dioxide Nanocrystals. *Science* **2011**, *331* (6018), 746−750.
(54) Yan, J.; Wu, G.; Guan, N.; Li, L.; Li, Z.; Cao, X. Understanding the Effect of Surface/Bulk Defects on the Photocatalytic Activity of TiO2: Anatase versus Rutile. *Phys. Chem. Chem. Phys.* **2013**, *15* (26), 10978−10988.
(55) Ren, R.; Wen, Z.; Cui, S.; Hou, Y.; Guo, X.; Chen, J. Controllable Synthesis and Tunable Photocatalytic Properties of Ti3+-Doped TiO2. *Sci. Rep.* **2015**, *5* (1), 10714.
(56) Yao, Y.; Cumberbatch, H.; Robertson, D. D.; Chin, M. A.; Lamkin, R.; Tolbert, S. H. On the Interplay between Size and Disorder in Suppressing Intercalation-Induced Phase Transitions in Pseudocapacitive Nanostructured MoS 2. *Adv. Funct. Mater.* **2024**, *34* (50), 2304896.
(57) Wang, J.; Polleux, J.; Lim, J.; Dunn, B. Pseudocapacitive Contributions to Electrochemical Energy Storage in TiO 2 (Anatase) Nanoparticles. *J. Phys. Chem. C* **2007**, *111* (40), 14925−14931.
(58) Chagnot, M.; Abello, S.; Wang, R.; Dawlaty, J.; Rodríguez-López, J.; Zhang, C.; Augustyn, V. Influence of Finite Diffusion on Cation Insertion-Coupled Electron Transfer Kinetics in Thin Film Electrodes. *J. Electrochem. Soc.* **2024**, *171* (1), 010527.
(59) Ohsaka, T.; Izumi, F.; Fujiki, Y. Raman Spectrum of Anatase, TiO 2. *J. Raman Spectrosc.* **1978**, *7* (6), 321−324.
(60) Tian, F.; Zhang, Y.; Zhang, J.; Pan, C. Raman Spectroscopy: A New Approach to Measure the Percentage of Anatase TiO 2 Exposed (001) Facets. *J. Phys. Chem. C* **2012**, *116* (13), 7515−7519.
(61) Louvain, N.; Henry, A.; Daenens, L.; Boury, B.; Stievano, L.; Monconduit, L. On the Electrochemical Encounter between Sodium and Mesoporous Anatase TiO2 as a Na-Ion Electrode. *CrystEngComm* **2016**, *18* (23), 4431−4437.
(62) Saeed, S.; Fleischmann, S.; Kobayashi, T.; Jusys, Z.; Mamontov, E.; Osti, N. C.; Holzapfel, N. P.; Song, H.; Wang, T.; Dai, S.; Jiang, D.; Augustyn, V. Oxide Acidity Modulates Structural Transformations in Hydrogen Titanates during Electrochemical Li-Ion Insertion. *J. Am. Chem. Soc.* **2024**, *146* (42), 28795−28808.
(63) Shirpour, M.; Cabana, J.; Doeff, M. New Materials Based on a Layered Sodium Titanate for Dual Electrochemical Na and Li Intercalation Systems. *Energy Environ. Sci.* **2013**, *6* (8), 2538.
(64) Bamberger, C. E.; Begun, G. M. Sodium Titanates: Stoichiometry and Raman Spectra. *J. Am. Ceram. Soc.* **1987**, *70* (3), C-48−C-51.
(65) Frenkel, D.; Smit, B. *Understanding Molecular Simulation: From Algorithms to Applications*; Elsevier, 2023.
(66) Hellenbrandt, M. The Inorganic Crystal Structure Database (ICSD) - Present and Future. *Crystallogr. Rev.* **2004**, *10* (1), 17−22.
(67) Anisimov, V. I.; Zaanen, J.; Andersen, O. K. Band Theory and Mott Insulators: Hubbard U Instead of Stoner I. *Phys. Rev. B* **1991**, *44* (3), 943−954.
(68) Sun, J.; Ruzsinszky, A.; Perdew, J. P. Strongly Constrained and Appropriately Normed Semilocal Density Functional. *Phys. Rev. Lett.* **2015**, *115* (3), 36402.
(69) Sai Gautam, G.; Carter, E. A. Evaluating Transition Metal Oxides within DFT-SCAN and $\text{SCAN}+U$ Frameworks for Solar Thermochemical Applications. *Phys. Rev. Mater.* **2018**, *2* (9), 95401.
(70) Long, O. Y.; Sai Gautam, G.; Carter, E. A. Evaluating Optimal U for $3d$ Transition-Metal Oxides within the SCAN+U Framework. *Phys. Rev. Mater.* **2020**, *4* (4), 45401.
(71) Perdew, J. P.; Burke, K.; Ernzerhof, M. Generalized Gradient Approximation Made Simple. *Phys. Rev. Lett.* **1996**, *77* (18), 3865−3868.
(72) Ong, S. P.; Richards, W. D.; Jain, A.; Hautier, G.; Kocher, M.; Cholia, S.; Gunter, D.; Chevrier, V. L.; Persson, K. A.; Ceder, G. Python Materials Genomics (Pymatgen): A Robust, Open-Source Python Library for Materials Analysis. *Comput. Mater. Sci.* **2013**, *68*, 314−319.
(73) Doebelin, N.; Kleeberg, R. {. \it Profex}: A Graphical User Interface for the Rietveld Refinement Program {\it BGMN. *J. Appl. Crystallogr.* **2015**, *48* (5), 1573−1580.
(74) Leinekugel-le-Cocq-Errien, A. Y.; Deniard, P.; Jobic, S.; Gautier, E.; Evain, M.; Aubin, V.; Bart, F. Structural Characterization of the Hollandite Host Lattice for the Confinement of Radioactive Cesium: Quantification of the Amorphous Phase Taking into Account the Incommensurate Modulated Character of the Crystallized Part. *J. Solid State Chem.* **2007**, *180* (1), 322−330.
(75) Kresse, G.; Furthmüller, J. Efficient Iterative Schemes for Ab Initio Total-Energy Calculations Using a Plane-Wave Basis Set. *Phys. Rev. B* **1996**, *54* (16), 11169−11186.
(76) Kresse, G.; Hafner, J. Ab Initio Molecular Dynamics for Open-Shell Transition Metals. *Phys. Rev. B* **1993**, *48* (17), 13115−13118.
(77) Kresse, G.; Joubert, D. From Ultrasoft Pseudopotentials to the Projector Augmented-Wave Method. *Phys. Rev. B* **1999**, *59* (3), 1758−1775.

https://doi.org/10.1021/acs.chemmater.6c00507
Chem. Mater. XXXX, XXX, XXX−XXX